

Identification of Allosteric Fingerprints of Alpha-Synuclein Aggregates in Matrix Metalloprotease-1 and Substrate-Specific Virtual Screening with Single Molecule Insights

Sumaer Kamboj

Colorado School of Mines

Chase Harms

Colorado School of Mines

Derek Wright

Colorado School of Mines

Anthony Nash

University of Oxford

Lokender Kumar

Colorado School of Mines

Judith Klein-Seetharaman

Colorado School of Mines

Susanta K. Sarkar (✉ ssarkar@mines.edu)

Colorado School of Mines

Research Article

Keywords: Interactions of MMP1 with aSyn aggregates, identification of substrate-specific allosteric fingerprints, substrate-dependent virtual screening.

Posted Date: December 9th, 2021

DOI: <https://doi.org/10.21203/rs.3.rs-1132741/v1>

License:  This work is licensed under a Creative Commons Attribution 4.0 International License.

[Read Full License](#)

Version of Record: A version of this preprint was published at Scientific Reports on April 6th, 2022. See the published version at <https://doi.org/10.1038/s41598-022-09866-7>.

Abstract

Alpha-synuclein (aSyn) has implications in pathological protein aggregations in neurodegeneration. Matrix metalloproteases (MMPs) are broad-spectrum proteases and cleave aSyn, leading to aggregation. Previously, we showed that allosteric communications between the two domains of MMP1 on collagen fibril and fibrin depend on substrates, activity, and ligands. Here we report quantification of allostery using single molecule measurements of MMP1 dynamics on aSyn-induced aggregates by calculating Förster Resonance Energy Transfer (FRET) between two dyes attached to the catalytic and hemopexin domains of MMP1. The two domains of MMP1 prefer open conformations that are inhibited by a single point mutation E219Q of MMP1 and tetracycline, an MMP inhibitor. A two-state Poisson process describes the interdomain dynamics, where the two states and kinetic rates of interconversion between them are obtained from histograms and autocorrelations of FRET values. Since a crystal structure of aSyn-bound MMP1 is not available, we performed molecular docking of MMP1 with aSyn using ClusPro. We simulated MMP1 dynamics using different docking poses and matched the experimental and simulated interdomain dynamics to identify an appropriate pose. We used experimentally validated simulations to define conformational changes at the catalytic site and identify allosteric residues in the hemopexin domain having strong correlations with the catalytic motif residues. We defined Shannon entropy to quantify MMP1 dynamics. We performed virtual screening against a site on selected aSyn-MMP1 binding poses and showed that lead molecules differ between free MMP1 and substrate-bound MMP1. Also, identifying aSyn-specific allosteric residues in MMP1 enabled further selection of lead molecules. In other words, virtual screening needs to take substrates into account for substrate-specific control of MMP1 activity. Molecular understanding of interactions between MMP1 and aSyn-induced aggregates may open up the possibility of degrading aggregates by targeting MMPs.

Introduction

Lewy bodies, intraneuronal cytoplasmic protein aggregates, are commonly observed in the brains of patients with Alzheimer's disease (AD) and Parkinson's disease (PD) (1). Alpha-synuclein (aSyn) is often the common protein detected in Lewy bodies observed in AD and PD (2). An established body of evidence shows that the C-terminal truncation of aSyn by proteases leads to protein aggregation and Lewy body formation. Both intracellular and extracellular proteolytic systems take part in the breakup of aSyn (3). The partial cleavage of aSyn explains aggregates due to fibrillation (4) and misfolding (5, 6). Although aggregates could be a consequence instead of a cause of AD and PD (7, 8), the uncontrolled aggregation will lead to cell death and worsening of effects (9, 10). As such, there is a need to find ways to degrade existing aggregates.

A growing body of evidence shows that matrix metalloproteases (MMPs) can partially cleave aSyn (11–15). Prior reports have shown that MMP1, MMP2, MMP3, MMP9, and MT1-MMP can partially cleave aSyn (13, 14) with the possible cleavage sites identified (13). MMPs are broad-spectrum proteases known to degrade extracellular matrix and non-matrix proteins (16, 17), but a growing body of evidence suggests proteolytic and non-proteolytic intracellular functions of MMPs (18). MMPs are found in extracellular

space (19), intracellular space (20), blood (21), intestine (22), brain (23) and can alter the blood-brain barrier (24). The implication of MMPs in partial cleavage of aSyn is significant because tetracycline (25, 26), a well-known inhibitor of MMPs (27), has shown therapeutic potential in AD (28) and PD (29). Thus, the broad-spectrum protease activity of MMPs not only leads to aSyn-induced aggregation, but it might also be useful in degrading existing aSyn-induced aggregates. However, it is not clear how MMPs might affect aSyn-induced aggregates, which are water-insoluble and challenging to study using standard biochemical assays. To this end, we have developed a single molecule tracking approach and weight-based activity assay to study water-soluble MMPs interacting with water-insoluble substrates. As such, it is possible to study MMP activity on aSyn-induced aggregates at the single molecule level.

However, it is not enough to know how MMP interacts with aggregates. Due to broad-spectrum activity, targeting MMPs for improving human health is challenging because MMPs interact with and degrade many proteins in the human body (30). Due to such diverse functions, any drug used for inhibiting MMPs results in adverse side effects (31). As such, there is only one FDA-approved MMP inhibitor (doxycycline hyclate) (32). To circumvent this problem, we need to understand the mechanisms behind diverse functions. The catalytic domain sequence of MMP1 is very similar to other MMPs in the family. However, the hemopexin domain sequence varies (33, 34), suggesting differences in activity and substrate specificity among MMPs due to long-distance communications (17, 35). Recently, we reported activity-dependent MMP1 dynamics and allosteric communications on type-1 collagen fibrils (36) and fibrin (37). We showed that functionally relevant conformations have the catalytic and hemopexin domains of MMP1 well-separated. These open conformations often accompany a larger catalytic pocket opening of MMP1, enabling the substrates to get closer to the active site of MMP1. Building on this, we have the opportunity to define dynamics and allosteric communications of MMP1 on aSyn-induced aggregates.

Quantifying dynamics and allosteric communications of MMP1 on a substrate involves quantifying randomness because proteins are inherently flexible biomolecules having both intra- and interdomain motions. Two types of randomness appear as proteins interact with their surroundings and substrates. First, the amino acids' locations and angles have a spatially random component at a particular time point. Second, as time progresses, proteins sample through different conformations leading to temporal randomness. Such correlated or collective fluctuations are essential for functions, including allosteric regulation (38–40), generation of mechanical work (41, 42), catalysis (43), ligand binding (44), and protein folding (45). Correlated motions decrease the conformational entropy and affect the kinetics and thermodynamics of biological processes (46). Shannon entropy is a quantitative measure to describe randomness in computer science and pattern recognition and quantify allostery in proteins to gain insights into their functional relevance (47–50).

In this paper, we report measurements of activity-dependent MMP1 interdomain dynamics on aSyn-induced aggregates of *E. coli* proteins at the single molecule level. MMP1 prefers open conformations on aSyn-induced aggregates, and these conformations are inhibited by tetracycline. A two-state Poisson process describes the interdomain dynamics of MMP1 on aggregates. Since aSyn-bound MMP1 crystal structures are not available, we used ClusPro for molecular docking of MMP1 with aSyn. We performed

all-atom simulations of different binding poses to calculate the interdomain dynamics and compare them with experimental dynamics. It appears that the pose with MMP1 bound to the middle U-shaped region of aSyn structure leads to dynamics similar to experimental dynamics. We used this pose to quantify allostery, define changes at the catalytic site, and identify functionally relevant allosteric residues. We also predicted the potential ligand binding sites and performed virtual screening against one of these binding sites to compare the lead molecules for free and aSyn-bound MMP1. Our results pave the way for substrate-dependent virtual screening guided by molecular insights that may enable inhibition of aggregation and degradation of aggregates.

Results And Discussion

MMP1 dynamics on aSyn-induced aggregates show activity-dependent conformations and correlations.

Figure 1A shows one of many binding poses between MMP1 and aSyn predicted by ClusPro (51). We purified catalytically active (E219) and inactive (Q219) MMP1 using a protease-based method described in our previous publication (52). Both active and inactive MMP1 had the SER142CYS mutation in the catalytic domain and SER366CYS mutation in the hemopexin domain for labeling with the Alexa555 (donor)-Alexa647 (acceptor) FRET pair. Labeling does not affect the activity of MMP1 (36). To distinguish the effects of enzymatic activity despite potential problems due to dyes' photophysical properties, we used the inactive MMP1 as a control. Since aSyn-induced aggregates are water-insoluble, we created a thin layer of aggregates on a quartz slide (**Figure 1B**). We flowed water-soluble MMPs to image the dynamics of MMP1 using a Total Internal Reflection Fluorescence (TIRF) microscope. We used a laser at 532 nm to excite Alexa555 (see methods). MMP1 undergoes interdomain dynamics and the distance between Alexa555 and Alexa647 changes. As a result, the non-radiative energy transfer due to FRET between the two dyes changes. Low FRET conformations lead to high Alexa555 emission, whereas high FRET conformations lead to low Alexa555 emission. Anticorrelated Alexa647 and Alexa555 emissions, I_A and I_D , respectively, indicate the conformational dynamics of MMP1 (**Figure 1C**). We calculated FRET using the equation $I_A/(I_A+I_D)$, where each FRET value determines the separation between the two MMP1 domains. We plotted the distribution of FRET values to assess MMP1 conformations on aSyn aggregates (**Figure 1D**). Active MMP1 prefers low FRET values in comparison to inactive MMP1, which suggests that MMP1 adopts open conformations on aSyn aggregates, similar to MMP1 conformations on collagen fibrils (36) and fibrin (37). In the presence of tetracycline, an MMP1 inhibitor (27), active and inactive MMP1 adopt similar conformations (**Figure 1E**), suggesting that tetracycline likely binds MMP1 to inhibit interdomain dynamics (36). We calculated the correlation (Equation 2 in methods) between conformations to determine how a conformation at one time is related to another conformation at a later time (**Figure 1F-G**). We fitted both power law and exponential distributions to the autocorrelations because these are the most common decay types of correlations. MMP1 dynamics have correlations on aSyn aggregates, and an exponential fits the correlations, which led to the identification of allosteric residues in MMP1 having strong correlations with the catalytic motif residues of MMP1 (see later).

A two-state Poisson process describes MMP1 dynamics on aSyn-induced aggregates. Recently, we published a quantitative analysis of MMP1 dynamics on collagen fibrils (36) and fibrin (37). The histograms reveal conformations of MMP1, and the autocorrelations show the relation between conformations at different time points. A sum of two Gaussians (Equation 1 in Methods) fits the histograms of smFRET values, and an exponential fits the autocorrelations (Equation 3 in methods). As such, a two-state Poisson process describes the conformational dynamics of MMP1 and enables a straightforward interpretation of the decay rates of correlations (36). We can establish a quantitative connection between the two states obtained from the Gaussian fits and the exponential fits' decay rates. We defined the two Gaussian centers as the two states, S1 (low FRET value) and S2 (high FRET value). Also, we described the two kinetic rates as k_1 ($S1 \leftrightarrow S2$) and k_2 ($S2 \leftrightarrow S1$) for interconversion between S1 and S2. For a two-state system, the ratio of rates (k_1/k_2) is the ratio of Gaussian area(S2)/area(S1), and the sum of rates (k_1+k_2) is the decay rate of autocorrelation. We calculated k_1 and k_2 from k_1/k_2 and k_1+k_2 for both active and inactive MMP1. Using experimentally determined S1, S2, k_1 , k_2 , and noise (widths of the histograms), we simulated smFRET trajectories and analyzed the simulated data similar to the experimental data. Comparing experimentally determined inputs (**Table S1**) and recovered parameters from two-state simulations (**Table S2**) shows that a two-state Poisson process describes MMP1 interdomain dynamics.

The two states are $S1=0.46$ and $S2=0.52$ on aSyn-induced aggregates for active MMP1 without ligand (**Table S1**). In comparison, the two states are $S1=0.44$ and $S2=0.55$ on collagen (36) and $S1=0.42$ and $S2=0.51$ on fibrin (37) for active MMP1 without ligand. The correlation decay rate of 0.08 s^{-1} on aSyn-induced aggregates for active MMP1 without ligand (**Table S1**). In comparison, the decay rates are 0.13 s^{-1} on collagen (36) and 0.08 s^{-1} on fibrin (37) for active MMP1 without ligand. In the presence of tetracycline, the two-state description still applies even though the two states and interconversion rates between them change (**Table S1**).

We performed two-state simulations with and without noise to study how noise affects the histograms and autocorrelations (**Figure 2A-F**). Only an exponential fits the autocorrelations with noise (**Figure 2D**). However, both power law and exponential fit the autocorrelations of simulated smFRET trajectories without noise (**Figure 2F**). In other words, the presence of noise can convert a power law correlation into an exponential correlation. This effect is similar to converting a Lorentzian line shape into a Gaussian line shape (53). An exponential fit recovers the simulated kinetic rates' underlying sum with and without noise (**Table S2**).

MMP1 dynamics depend on the aSyn-MMP1 binding pose. Since crystal structures of aSyn-bound MMP1 do not exist, we predicted the binding poses of aSyn (PDB ID 1XQ8) and MMP1 (PDB ID 4AUO) computationally using molecular docking software ClusPro (51, 54). **Figures 3A-C** show three such binding poses. MMP1 cleaves aSyn and produces several fragments, including fragments with amino acids 1-21, 1-41, 1-47, 1-133, 1-134, 8-140, 19-140, 71-140, 72-140, 79-140, 91-140, and 98-140 (13). We selected three poses based on these cleavage fragments of aSyn near amino acids 45 (pose 3), 75 (pose 2), and 91 (pose 1). We leveraged known cleavage sites of MMP1 because the computational binding

energy may not be the best indicator of appropriate docking poses (55). We performed all-atom MD simulations for the three binding poses (**Figure 3**) and calculated the catalytic pocket opening (**Figures 3D-F**) and interdomain separation (**Figures 3G-I**) of MMP1. Since MMP1 stabilized within ~5 ns (**Figure S2**), we performed simulations for 20 ns. We chose pose 3 for further investigation because the distribution of interdomain distance (**Figure 3I**) shows a similarity with the experimental distribution (**Figure 1D**).

Additionally, we performed experiments on aSyn aggregates, and aggregation occurs due to C-terminal fragmentation, and as such, pose 3 presents a vulnerable position for MMP1 activity on aggregates. Aggregation may also reduce the intrinsic disorder of aSyn by forming structured fibrils (56). Nevertheless, there are two important caveats. First, we performed simulations on aSyn monomer but performed experiments on aggregates. We took a similar approach for collagen and found that simulations on collagen monomer agreed with experiments on collagen fibril when we restrained the collagen backbone (36), suggesting strains in collagen monomers inside collagen fibrils. For aSyn, we did not have to restrain the aSyn backbone for agreement between simulations and experiments, suggesting a lack of strain in aSyn-induced aggregates. Second, aSyn is considered an intrinsically disordered protein (57) that assumes a structure after binding substrate (58) or forming aggregates. Also, aSyn purified from neuronal and non-neuronal cell lines generally suggests a "natively folded" ~58 kDa tetrameric form (59, 60). Nevertheless, the combined experiment-simulation approach using the monomer structure of aSyn provides a starting point for molecular-level understanding.

Shannon entropy enables the quantification of allosteric communications. Since a correlated motion suggests a decrease in randomness or lower entropy, we calculated correlations between each pair of residues in MMP1 and estimated entropy (**Figure 4**). We divided all-atom simulations into 1 ns long windows. In each 1 ns window, there were 200 radial coordinates for residues. We calculated correlations of fluctuations (Equation 2 in methods) and normalized it to a range of 0 to 1 by subtracting the minimum and then dividing by the maximum. **Figures 4A-C** show the matrix of correlation values at lag number 1, averaged over 20 ns (see supplementary information for the meaning of lag numbers and correlation calculations). We divided the correlation values to create 10 bins of width 0.1, calculated 10·10 gray-level co-occurrence matrix (GLCM), and defined Shannon entropy $S = - \sum p_i \ln p_i$, where p_i is the probability of a microstate. The catalytic domain residues (F100-Y260) have strong correlations with the hemopexin domain residues (D279-C466), suggesting allosteric communications in MMP1 (**Figures 4A-C**). The time-evolutions of Shannon entropy are shown in **Figures 4D-F**. Pose 3 has the lowest entropy consistent with the functionally relevant binding pose.

We performed MD simulations of pose 3 at 22 °C to compare with smFRET measurements at 22 °C. **Figure 5A** shows the distributions of the interdomain distance between S142 and S366. In agreement with experiments (**Figure 1D**), active MMP1 adopts conformations with the two domains separated more than inactive MMP1. Also, simulated dynamics correlations (**Figure 5B**) follow the experimental pattern (**Figure 1F**), with inactive MMP1 having higher values with longer correlation times. We used experimentally consistent simulations to gain further insights. First, the correlation between the catalytic

pocket opening and interdomain separation for active MMP1 is higher than inactive MMP1 (**Figure 5C**). A larger catalytic pocket opening enables substrates to get closer to the active site. Second, the two-dimensional correlation plots show allosteric communications between the two domains (**Figures 5D-E**). Third, Shannon entropy describing the randomness of two-dimensional correlations plots shows a lower value for active MMP1 than inactive MMP1 (**Figure 5F**).

We also repeated simulations of pose 3 at 22 °C with two zinc and four calcium ions in MMP1 (**Figure S4**). Two main insights remain the same with and without ions. First, active MMP1 prefers an open conformation (more separation between domains or low FRET), which is consistent with experiments (**Figure 1D**), 100 ns simulations with ions (**Figure S4A**), and 20 ns simulations without ions (**Figure 5A**). Second, MMP1 has strong allosteric communications between domains, which is consistent with 100 ns simulations with ions (**Figures S4D-E**) and 20 ns simulations without ions (**Figures 5D-E**). Although ions, especially the catalytic Zn, are critical for the final hydrolysis step by MMPs, they may be less influential on structural dynamics (61).

Since we obtained similar insights with and without metal ions, we performed all other simulations without metal ions. Without metal ions, validated force field parameters for the 20 natural amino acids are already available and can be used for molecular dynamics simulations of any protein with a structure. However, the force field parameters for metal ions must be calculated for each case because these parameters depend upon the nature of the metal ion, its coordination number, and its geometrical arrangement (62). As such, molecular dynamics simulations with metal ions are more complicated and time-intensive, and we performed simulations without metal ions.

Changes at the catalytic site and identification of allosteric residues in MMP1. We performed MD simulations for free MMP1 (**Figure 6A**) and compared them with the simulations (**Figure 4C**) for pose 3 (**Figure 3C**) of aSyn-bound MMP1. The comparison revealed how the conformations of MMP1 catalytic motif HELGHSLGLSH changed. We considered the catalytic residue E219 as the origin, calculated the average (x,y,z) coordinates of all atoms in each amino acid to define the amino acid's location, and plotted the pairwise distance with the catalytic motif residues in three dimensions. The symbol size of the locations is proportional to the standard deviation of the pairwise distance (**Figure 6B**). The configuration at the MMP1 catalytic site changes considerably as free MMP1 binds aSyn.

We plotted histograms of correlation values for free and aSyn-bound MMP1 and determined the threshold correlation values at 0.8 (peak probability density ~ 2.2 divided by 2.7) (**Figure 6C**). We found all the residues having normalized correlations greater than 0.8 in **Figure 4C** and **Figure 6A** with the catalytic motif residues HELGHSLGLSH and compared the residues between free MMP1 and aSyn-bound MMP1. We identified residues in the hemopexin domain between D279 and C466 having exclusive correlations with the catalytic motif residues only MMP1 binds aSyn. These residues are 281, 283, 292, 327, 328, 329, 337, 343, 345, 346, 348, 353, 354, 363, 365, 366, 367, 368, 371, 372, 374, 375, 379, 391, 394, 399, 414, 419, 426, and 466. **Figure S6** shows these allosteric residues in MMP1, some of which are surface exposed and, as such, can be targeted for virtual screening. Identifying allosteric residues is significant

because it may be possible to identify exclusive residues for other substrates of MMP1 and control one MMP1 function without affecting the other functions.

Lead molecules from virtual screening against MMP1 depend on the binding pose. Guided by experiments and simulations, we determined that pose 3 is likely a relevant binding pose between MMP1 and aSyn. Therefore, we used the experimentally-informed binding pose for the virtual screening of molecules. Virtual screening enables testing considerably more ligands economically and faster than high-throughput experimental screening. A wide range of strategies can be divided into ligand-based and structure-based virtual screening (63). In ligand-based virtual screening, known ligands against a target serve as benchmarks to screen for more ligands with similar properties. In contrast, structure-based screening uses the binding sites on a target to screen molecules leveraging the conformational changes and energetic complementarity upon ligand binding. Since MMP1 has broad-spectrum protease activity, we determined the binding sites on free MMP1 and aSyn-bound MMP1 to investigate a substrate's effects. We predicted the potential ligand-binding sites using AutoLigand and MGLTools 1.5.7 and selected a potential binding site in the hemopexin domain having significant overlap with the identified allosteric residues in the last paragraph (**Figure 7A**).

We performed screening against the selected site in the hemopexin domain for free MMP1 and two poses of aSyn-bound MMP1. We performed molecular docking using AutoDock (64) and set up the virtual screening with Raccoon 1.1. We used default AutoDock docking parameters (see supplementary information) to determine the binding affinities for a collection of 1,400 FDA-approved compounds from the ZINC15 database (65). We used FDA-approved molecules because those provide a smaller set of commercially available molecules. We fixed the otherwise flexible side chains. Flexible side chains would have given slightly more accurate screening but would require more computational time. We found that the lead molecules against MMP1 change depending on the substrate and pose. **Figures 7B-D** show the top molecules for free MMP1 and the two aSyn-MMP1 binding poses, suggesting that substrate binding and different poses can lead to different results. Venn diagrams of molecules (**Figures 7B-C**) show that there are molecules unique to each case. The ligand-binding site in the hemopexin domain was common to free MMP1, pose 1, and pose 3. However, conformational differences in the three cases clearly impact virtual screening. The unique molecules for each case suggest that we should perform substrate-specific screening to identify unique ligands, thus resolving problems arising from MMP promiscuity.

Substrate-specific allosteric residues in MMP1 enable single molecule insights into the selection of lead molecules. As a proof of principle, we wanted to check if aSyn-specific allosteric residues may help the selection of drugs because aSyn has its unique signature or "fingerprint" on MMP1 at the catalytic and distant allosteric sites. To this end, we screened ~9000 FDA-approved drugs (see methods) from the ZINC15 database and selected compounds for which the difference between the binding affinities at the top two binding modes is at least 10% because we want to find drugs that bind preferably to a specific site on MMP1. With a 10% difference, we found ~600 drugs out of ~9000 starting drugs. We considered the top affinity site for each compound, identified the MMP1 residue closest to each drug, and plotted it in 2D (**Figure 8A**). Then, we selected drugs further by identifying drugs binding to the aSyn-specific allosteric

residues (**Figures 8B**), leading to only a few lead molecules. **Figure 8C** shows how Palbociclib binds to an aSyn-specific MMP1 residue. These results suggest that we may be able to identify drugs with an exclusive binding preference for an allosteric site on MMP1 by screening a larger number of compounds, potentially reducing off-target effects. Since MMPs interact with and degrade many biomolecules in the human body, substrate-specific allosteric residues or "allosteric fingerprints" may alter one MMP1 function without affecting its other activities using allosteric ligands.

Conclusions

In summary, we measured the interdomain dynamics of MMP1 on aSyn-induced protein aggregates and modeled the dynamics as a two-state Poisson process. Distributions of conformations and correlation decay rates of MMP1 on aSyn-induced aggregates follow the general pattern that we previously reported for collagen (36) and fibrin (37), i.e., open MMP1 conformations are functionally relevant, and there are time-dependent correlations of conformations.

A comparison of experiments and simulations suggested that the pose in which MMP1 binds to aSyn near amino acid 45 (pose 3) leads to a better match with experiments. Simulations further suggested that the configuration of the catalytic motif HELGHSLGLSH differs significantly between free and aSyn-bound MMP1. We identified allosteric residues in the hemopexin domain between D279 and C466, having strong correlations with the catalytic motif residues. These allosteric residues in the hemopexin domain may enable engineering MMP1 activity due to their strong correlations with the catalytic motif.

We found that the potential ligand-binding sites change upon binding aSyn and depend on the binding pose. The lead molecules and their scores against the selected site having significant overlap with identified allosteric residues change upon binding the substrate and depend on the binding pose. Therefore, substrate-dependent binding sites and lead molecules suggest that any effort to target MMP1 may need to consider the substrate, the binding pose, and the ligand-binding site. The synergistic combination of experiments and simulations enables modulation of MMP1 activity using molecular insights at the single molecule level. It may pave the way for substrate-specific control of MMP activity using allosteric ligands.

Materials And Methods

Purification of MMP1 and aSyn. The MMP1 and aSyn sequences were inserted into the pET21b+ and pET11a vectors, respectively, between NdeI (N-terminal) and HindIII (C-terminal) restriction sites. We transformed the plasmids into Rosetta (DE3) pLysS *E. coli* (Millipore, Cat# 70956-4) for protein expression. We purified MMP1 and aSyn, as described in our previous publications (52, 66). The method of purifying aSyn also produced aSyn-induced aggregates used in experiments.

Measurements of MMP1 interdomain dynamics. For smFRET measurements of MMP1 interdomain dynamics, we mutated two serine residues in MMP1 at locations 142 and 366 to cysteines for labeling

with Alexa555 and Alexa647 dyes. In addition, we introduced the E219Q mutation in the catalytic domain to create a catalytically inactive mutant of MMP1. We spread aSyn-induced aggregates and made a thin layer on a quartz slide. We made a flow cell for single molecule experiments using a piece of double-sided adhesive tape sandwiched between the quartz slide and a glass coverslip. Labeled MMPs were flowed into the flow cell and excited at 532 nm wavelength using the evanescent wave created at the quartz slide and sample buffer interface in a TIRF microscope. We acquired two-channel movies to detect emissions from Alexa555 and Alexa647. Any relative motion between the two MMP1 domains would lead to a non-radiative transfer of energy from Alexa555 to Alexa647 due to FRET, increasing the emission from Alexa647 (I_A) and simultaneously reducing the emission from Alexa555 (I_D). We calculated FRET efficiency by $I_A / (I_A + I_D)$ (67). Single-molecule experiments and analyses have been described in our previous publications (68–71).

All-atom simulations without metal ions. We removed all zinc and calcium ions and the water molecules from PDB ID 4AU0 and replaced the missing side-chain atoms using Chimera's rotamer tool. The PDB files for active and inactive MMP1 were created by replacing A219 with E219 and Q219, respectively, using Pymol's mutagenesis function. We used Gromacs 2019.6 with the Gromos96 43a1 force field to perform the MD simulations. We ignore the hydrogen atoms while creating the topology file. Each simulation ran 20 ns long, simulated at 2 fs/step, and sampled every 5 ps. Each MMP1 crystal was placed in a cubic box with 3D period boundary conditions and solvated with water (using a single point charge model (SPC)) and Na counter-ions to create a neutral system. We then used the steepest descent algorithm to minimize the solution's energy. To equilibrate the solution with the protein complex, we used NVT and NPT ensemble simulations. First, we performed the NVT simulation and set the mean temperature at the desired temperature of 295 K (22 °C) or 310 K (37 °C) using a Berendsen thermostat for 100 ps. We used the Verlet cut-off scheme for neighbor searching and updated the neighbor list every 20 fs. We used the particle mesh Ewald scheme to calculate the electrostatic interactions with a cubic interpolation order of 4 and a cut-off at 1 nm. We assigned initial velocities using a Maxwell distribution from the corresponding temperature. In the NPT simulation, we maintained velocities from the NVT simulation output, and the pressure was set to 1 bar using a Parrinello-Rahman barostat for an additional 100 ps. Once the NVT and NPT simulations were finished, and the system was equilibrated, we removed the position restraints and ran the production MD for 20 ns. We edited the final coordinates in the trajectory file to correct for periodicity and center the protein complex. The distances between the catalytic pocket residues and the serine residues (interdomain distance) are then measured at every time step using the Gromacs distance function. We measured the interdomain separation between the alpha carbon atoms of residues S142 and S366 and the catalytic pocket opening between the alpha carbon atoms of residues N171 and T230. To calculate the correlation and Shannon entropy, we recorded the alpha carbon atom's coordinates in each residue of MMP1.

Analysis of experimental and simulated interdomain dynamics. We chose the histograms' bin width to be at least the inverse of the sample size's square root, i.e., $1 / \sqrt{N}$, N is the number of data points. We calculated the error of count in each bin as the square root of the bin count. Both the bin counts and

errors were divided by the histogram area to create the area-normalized histogram (probability density function). The area under the normalized histogram equals 1. We fitted a sum of two Gaussians to the histograms:

$$y = a_1 \times e^{-\frac{(x-b_1)^2}{c_1^2}} + a_2 \times e^{-\frac{(x-b_2)^2}{c_2^2}} \quad (1)$$

where a's, b's, and c's are amplitudes, centers, and widths of the Gaussians. The parameters b1 and b2 are the two states, S1 and S2.

To calculate correlations, we subtracted the average value from each trajectory and used the following equation to calculate correlations:

$$C_\tau = \frac{1}{N-\tau} \sum_{t=1}^{N-\tau} \left\{ I(t) - \frac{1}{N-\tau} \sum_{t'=1}^{N-\tau} I(t') \right\} \times \left\{ I(t+\tau) - \frac{1}{N-\tau} \sum_{t'=1+\tau}^N I(t') \right\} \quad (2)$$

where C_τ is the correlation at lag number τ , N is the number of points in a FRET trajectory, and $I(t)$ is the FRET value at t . For autocorrelations, both factors in curly brackets were from the same time series. For cross-correlations, the two factors in curly brackets were from different time series.

We normalized correlations by dividing correlation values at each lag by $C_{\tau=0}$. We fitted correlations between $\tau = 1$ and $\tau = 1000$ to both power law and exponential distributions. For power law, we used a form of Pareto distribution (72) that satisfies the boundary conditions, i.e., $C_{\tau=0} = 1$ at $t = 0$ and $C_{\tau=\infty} = 0$ at $t = \infty$.

We fitted the following equations of power law and exponential functions:

$$C_\tau = (a \times \tau + 1)^{-b} \quad (3)$$

$$C_\tau = d \times \exp^{-e \times \tau} + f$$

To quantify linear correlations between the catalytic pocket opening and interdomain separation from simulations, we used the interdomain distance as the single predictor variable for the catalytic pocket distance in a linear model. A linear model describes a response variable as a function of predictor variables. Linear models are often fit using a method known as a statistical regression. There are different regression methods used, depending on the number of predictor variables. When using only one predictor variable, the regression method is known as the simple linear regression, which we used for quantifying correlations. We used the following equation:

$$y_i = b_0 + b_1 \times x_i \quad (4)$$

where b_0 and b_1 are the estimated fit parameters. There are also a few different methods to estimate the parameters of the linear model. The most-used approach is the least-squares operator, which finds the slope through the data that minimizes the squared distance between the fit and the residues. There is still uncertainty in these estimations, no matter which method we used. Confidence bands visually represent the uncertainty in linear models by showing the range of possible slopes. We calculated the 95% confidence interval of each predictor value's mean.

Small molecule putative binding sites on MMP1. For virtual screening, we selected free MMP1 and two poses of aSyn-MMP1 binding. First, we predicted potential putative binding sites using AutoLigand and MGLTools 1.5.7. Next, we assigned hydrogen atoms (including polar hydrogens) and Gasteiger partial charges to each of the two aSyn-bound MMP1 poses and free MMP1. Zinc and calcium ions were removed. A grid map with 1Å spacing was then applied to the hemopexin and catalytic domains in addition to the linker region, making the docking unbiased for different binding sites, especially allosteric ones. AutoLigand was then used to define four binding site calculations per structure, beginning with 100 points to define the volume of the binding envelope, then increasing the number of points to 200, 300, and finally 400. The binding envelopes defined were analyzed using AutoDock, and results were visualized using MGLTools and VMD.

Pose-dependent virtual screening of small molecules against a putative site on MMP1. We performed molecular docking using AutoDock, and the virtual screening was set up with Raccoon 1.1. The receptor was considered rigid, and rotatable bonds imparted flexibility to the ligands. We used default AutoDock docking parameters (see supplementary information) to determine the small-molecule binding affinities. A collection of 1,400 FDA-approved compounds were obtained from the ZINC15 database. We began by importing the ligand multiple structure MOL2 file into Raccoon. Each ligand was automatically converted into a separate PDBQT while settling hydrogen atoms and partial charges. We calculated a set of new grid map files with a grid spacing of 0.37Å to include the selected putative binding site from the binding site prediction. For each of the three cases (free MMP1 and two aSyn-MMP1 poses), 100 ligands with the lowest binding affinities were identified. The lead molecules' ZINC IDs were converted to chemical IDs (CIDs) for comparison. The top 10 ligands were identified by their common names.

Single molecule insights into the virtual screening. We used free MMP1 and binding pose 3 of aSyn-bound MMP1 as the receptors. We opened PDB files of MMP1 in AutoDockTools, added polar hydrogens, and created a .pdbqt file for the three receptors, i.e., free MMP1 and aSyn-bound MMP1. We selected ~9000 FDA-approved compounds from the ZINC15 database and downloaded the selected compounds as a .sdf file for ligands. We used OpenBabel to convert the .sdf file into a .pdbqt file, then AutoDock Vina to create individual .pdbqt files using vina_split on a Linux terminal. We also made a .txt file containing filenames for the compounds. We created a configuration file to set the parameters of screening in AutoDock Vina. The configuration file is a .txt file containing receptors' filename, docking box coordinates,

number of modes, energy range, and exhaustiveness. We used the AutoDockTools GUI to obtain the coordinates by opening the Grid menu and selecting Grid Box. We adjusted the box to enclose the whole MMP1 to identify the binding poses of each compound and used an exhaustiveness of 10 for quicker screening. After the virtual screening, we obtained two types of files: a .pdbqt file of the top 10 docking modes and a log of their binding affinity scores. We analyzed the results in Matlab.

Declarations

Acknowledgments

One grant to S.K.S. and J.K.S. from the National Institutes of Health (R15 GM137295) partially supported this work. A. N. is funded by the NIHR Oxford Health NHS Foundation Trust Biomedical Research Centre. This work was supported in part through the computational resources provided by Science Outreach Servers.

Author contributions

S.K.S. conceived and designed the overall project, S.K. performed experiments, L.K. collected single molecule data, C.H. and D.W. performed all-atom simulations without ions and virtual screening, D.W. performed Shannon entropy calculations, A.N. performed MD simulations with ions and virtual screening, S.K., C.H., D.W., A.N., J.K.S., and S.K.S. analyzed data. S.K.S. wrote the manuscript. All authors edited the manuscript.

Competing financial interests

The authors declare no competing financial interests.

References

1. Parkkinen, L., T. Pirttilä, and I. Alafuzoff. 2008. Applicability of current staging/categorization of α -synuclein pathology and their clinical relevance. *Acta neuropathologica* 115(4):399-407.
2. Spillantini, M. G., M. L. Schmidt, V. M.-Y. Lee, J. Q. Trojanowski, R. Jakes, and M. Goedert. 1997. α -Synuclein in Lewy bodies. *Nature* 388(6645):839.
3. Xilouri, M., O. R. Brekk, and L. Stefanis. 2013. Alpha-synuclein and protein degradation systems: a reciprocal relationship. *Molecular neurobiology* 47(2):537-551.
4. Horvath, I., C. F. Weise, E. K. Andersson, E. Chorell, M. Sellstedt, C. Bengtsson, A. Olofsson, S. J. Hultgren, M. Chapman, and M. Wolf-Watz. 2012. Mechanisms of protein oligomerization: inhibitor of functional amyloids templates α -synuclein fibrillation. *Journal of the American Chemical Society* 134(7):3439-3444.
5. Selkoe, D. J. 2004. Cell biology of protein misfolding: the examples of Alzheimer's and Parkinson's diseases. *Nature cell biology* 6(11):1054.

6. Forloni, G., L. Terreni, I. Bertani, S. Fogliarino, R. Invernizzi, A. Assini, G. Ribizzi, A. Negro, E. Calabrese, and M. A. Volonté. 2002. Protein misfolding in Alzheimer's and Parkinson's disease: genetics and molecular mechanisms. *Neurobiology of aging* 23(5):957-976.
7. Espay, A. J., J. A. Vizcarra, L. Marsili, A. E. Lang, D. K. Simon, A. Merola, K. A. Josephs, A. Fasano, F. Morgante, and R. Savica. 2019. Revisiting protein aggregation as pathogenic in sporadic Parkinson and Alzheimer diseases. *Neurology* 92(7):329-337.
8. Lansbury, P. T., and H. A. Lashuel. 2006. A century-old debate on protein aggregation and neurodegeneration enters the clinic. *Nature* 443(7113):774-779.
9. Ross, C. A., and M. A. Poirier. 2004. Protein aggregation and neurodegenerative disease. *Nature medicine* 10(7):S10-S17.
10. Irvine, G. B., O. M. El-Agnaf, G. M. Shankar, and D. M. Walsh. 2008. Protein aggregation in the brain: the molecular basis for Alzheimer's and Parkinson's diseases. *Molecular medicine* 14(7):451-464.
11. Mizoguchi, H., K. Yamada, and T. Nabeshima. 2011. Matrix metalloproteinases contribute to neuronal dysfunction in animal models of drug dependence, Alzheimer's disease, and epilepsy. *Biochemistry research international* 2011.
12. Leake, A., C. Morris, and J. Whateley. 2000. Brain matrix metalloproteinase 1 levels are elevated in Alzheimer's disease. *Neuroscience letters* 291(3):201-203.
13. Levin, J., A. Giese, K. Boetzel, L. Israel, T. Högen, G. Nübling, H. Kretschmar, and S. Lorenzl. 2009. Increased α -synuclein aggregation following limited cleavage by certain matrix metalloproteinases. *Experimental neurology* 215(1):201-208.
14. Sung, J. Y., S. M. Park, C.-H. Lee, J. W. Um, H. J. Lee, J. Kim, Y. J. Oh, S.-T. Lee, S. R. Paik, and K. C. Chung. 2005. Proteolytic cleavage of extracellular secreted α -synuclein via matrix metalloproteinases. *Journal of Biological Chemistry* 280(26):25216-25224.
15. Rosenberg, G. A. 2009. Matrix metalloproteinases and their multiple roles in neurodegenerative diseases. *The Lancet Neurology* 8(2):205-216.
16. Rodríguez, D., C. J. Morrison, and C. M. Overall. 2010. Matrix metalloproteinases: what do they not do? New substrates and biological roles identified by murine models and proteomics. *Biochimica et Biophysica Acta (BBA)-Molecular Cell Research* 1803(1):39-54.
17. Morrison, C. J., G. S. Butler, D. Rodríguez, and C. M. Overall. 2009. Matrix metalloproteinase proteomics: substrates, targets, and therapy. *Current opinion in cell biology* 21(5):645-653.
18. Jobin, P. G., G. S. Butler, and C. M. Overall. 2017. New intracellular activities of matrix metalloproteinases shine in the moonlight. *Biochimica et Biophysica Acta (BBA)-Molecular Cell Research* 1864(11):2043-2055.
19. Lukes, A., S. Mun-Bryce, M. Lukes, and G. A. Rosenberg. 1999. Extracellular matrix degradation by metalloproteinases and central nervous system diseases. *Molecular neurobiology* 19(3):267-284.
20. Cauwe, B., and G. Opdenakker. 2010. Intracellular substrate cleavage: a novel dimension in the biochemistry, biology and pathology of matrix metalloproteinases. *Critical reviews in biochemistry and molecular biology* 45(5):351-423.

21. Zucker, S., M. Hymowitz, C. Conner, H. M. Zarrabi, A. N. Hurewitz, L. Matrisian, D. Boyd, G. Nicolson, and S. Montana. 1999. Measurement of matrix metalloproteinases and tissue inhibitors of metalloproteinases in blood and tissues: clinical and experimental applications. *Annals of the New York Academy of Sciences* 878(1):212-227.
22. Schuppan, D., and E. Hahn. 2000. MMPs in the gut: inflammation hits the matrix. *Gut* 47(1):12-14.
23. Dzwonek, J., M. Rylski, and L. Kaczmarek. 2004. Matrix metalloproteinases and their endogenous inhibitors in neuronal physiology of the adult brain. *FEBS letters* 567(1):129-135.
24. Rempe, R. G., A. M. Hartz, and B. Bauer. 2016. Matrix metalloproteinases in the brain and blood–brain barrier: versatile breakers and makers. *Journal of Cerebral Blood Flow & Metabolism* 36(9):1481-1507.
25. Greenwald, R., L. Golub, N. Ramamurthy, M. Chowdhury, S. Moak, and T. Sorsa. 1998. In vitro sensitivity of the three mammalian collagenases to tetracycline inhibition: relationship to bone and cartilage degradation. *Bone* 22(1):33-38.
26. Federici, T. J. 2011. The non-antibiotic properties of tetracyclines: clinical potential in ophthalmic disease. *Pharmacological research* 64(6):614-623.
27. Acharya, M. R., J. Venitz, W. D. Figg, and A. Sparreboom. 2004. Chemically modified tetracyclines as inhibitors of matrix metalloproteinases. *Drug Resistance Updates* 7(3):195-208.
28. Balducci, C., and G. Forloni. 2019. Doxycycline for Alzheimer's disease: fighting β -amyloid oligomers and neuroinflammation. *Frontiers in pharmacology* 10.
29. Bortolanza, M., G. C. Nascimento, S. B. Socias, D. Ploper, R. N. Chehín, R. Raisman-Vozari, and E. Del-Bel. 2018. Tetracycline repurposing in neurodegeneration: focus on Parkinson's disease. *Journal of Neural Transmission* 125(10):1403-1415.
30. Nuti, E., T. Tuccinardi, and A. Rossello. 2007. Matrix metalloproteinase inhibitors: new challenges in the era of post broad-spectrum inhibitors. *Current pharmaceutical design* 13(20):2087-2100.
31. Mohan, V., D. Talmi-Frank, V. Arkadash, N. Papo, and I. Sagi. 2016. Matrix metalloproteinase protein inhibitors: highlighting a new beginning for metalloproteinases in medicine. *Metalloproteinases in medicine* 3:31-47.
32. Sloan, B., and N. Scheinfeld. 2008. The use and safety of doxycycline hyclate and other second-generation tetracyclines. *Expert opinion on drug safety* 7(5):571-577.
33. Eckhard, U., P. F. Huesgen, O. Schilling, C. L. Bellac, G. S. Butler, J. H. Cox, A. Dufour, V. Goebeler, R. Kappelhoff, and U. auf dem Keller. 2016. Active site specificity profiling of the matrix metalloproteinase family: Proteomic identification of 4300 cleavage sites by nine MMPs explored with structural and synthetic peptide cleavage analyses. *Matrix Biology* 49:37-60.
34. Ratnikov, B. I., P. Cieplak, K. Gramatikoff, J. Pierce, A. Eroshkin, Y. Igarashi, M. Kazanov, Q. Sun, A. Godzik, and A. Osterman. 2014. Basis for substrate recognition and distinction by matrix metalloproteinases. *Proceedings of the National Academy of Sciences* 111(40):E4148-E4155.
35. Overall, C. M. 2002. Molecular determinants of metalloproteinase substrate specificity. *Molecular biotechnology* 22(1):51-86.

36. Kumar, L., A. Nash, C. Harms, J. Planas-Iglesias, D. Wright, J. Klein-Seetharaman, and S. K. Sarkar. 2020. Allosteric Communications between Domains Modulate the Activity of Matrix Metalloprotease-1. *Biophysical Journal* 119(2):360-374.
37. Kumar, L., J. Planas-Iglesias, C. Harms, S. Kamboj, D. Wright, J. Klein-Seetharaman, and S. K. Sarkar. 2020. Activity-dependent interdomain dynamics of matrix metalloprotease-1 on fibrin. *Scientific Reports* 10(1):1-14.
38. Goodey, N. M., and S. J. Benkovic. 2008. Allosteric regulation and catalysis emerge via a common route. *Nature chemical biology* 4(8):474.
39. Hammes, G. G. 2002. Multiple conformational changes in enzyme catalysis. *Biochemistry* 41(26):8221-8228.
40. Kern, D., and E. R. Zuiderweg. 2003. The role of dynamics in allosteric regulation. *Current opinion in structural biology* 13(6):748-757.
41. Vale, R. D., and R. A. Milligan. 2000. The way things move: looking under the hood of molecular motor proteins. *Science* 288(5463):88-95.
42. Schliwa, M., and G. Woehlke. 2003. Molecular motors. *Nature* 422(6933):759-765.
43. Hammes-Schiffer, S., and S. J. Benkovic. 2006. Relating protein motion to catalysis. *Annu. Rev. Biochem.* 75:519-541.
44. Csermely, P., R. Palotai, and R. Nussinov. 2010. Induced fit, conformational selection and independent dynamic segments: an extended view of binding events. *Trends in biochemical sciences* 35(10):539-546.
45. Sugita, Y., and Y. Okamoto. 1999. Replica-exchange molecular dynamics method for protein folding. *Chemical physics letters* 314(1-2):141-151.
46. Jarymowycz, V. A., and M. J. Stone. 2006. Fast time scale dynamics of protein backbones: NMR relaxation methods, applications, and functional consequences. *Chemical reviews* 106(5):1624-1671.
47. Schreiber, T. 2000. Measuring information transfer. *Physical review letters* 85(2):461.
48. Kamberaj, H., and A. van der Vaart. 2009. Extracting the causality of correlated motions from molecular dynamics simulations. *Biophysical journal* 97(6):1747-1755.
49. Burger, V. M., D. J. Arenas, and C. M. Stultz. 2016. A structure-free method for quantifying conformational flexibility in proteins. *Scientific reports* 6:29040.
50. Lenaerts, T., J. Ferkinghoff-Borg, F. Stricher, L. Serrano, J. W. Schymkowitz, and F. Rousseau. 2008. Quantifying information transfer by protein domains: analysis of the Fyn SH2 domain structure. *BMC structural biology* 8(1):43.
51. Kozakov, D., D. R. Hall, B. Xia, K. A. Porter, D. Padhorny, C. Yueh, D. Beglov, and S. Vajda. 2017. The ClusPro web server for protein–protein docking. *Nature protocols* 12(2):255.
52. Kumar, L., W. Colomb, J. Czerski, C. R. Cox, and S. K. Sarkar. 2018. Efficient protease based purification of recombinant matrix metalloprotease-1 in *E. coli*. *Protein expression and purification*

148:59-67.

53. Wertheim, G., M. Butler, K. West, and D. Buchanan. 1974. Determination of the Gaussian and Lorentzian content of experimental line shapes. *Review of Scientific Instruments* 45(11):1369-1371.
54. Comeau, S. R., D. W. Gatchell, S. Vajda, and C. J. Camacho. 2004. ClusPro: a fully automated algorithm for protein–protein docking. *Nucleic acids research* 32(suppl_2):W96-W99.
55. Yanamala, N., K. C. Tirupula, and J. Klein-Seetharaman. 2008. Preferential binding of allosteric modulators to active and inactive conformational states of metabotropic glutamate receptors. In *BMC bioinformatics*. BioMed Central. S16.
56. Lashuel, H. A. 2020. Do Lewy bodies contain alpha-synuclein fibrils? and Does it matter? A brief history and critical analysis of recent reports. *Neurobiology of disease* 141:104876.
57. Drescher, M., M. Huber, and V. Subramaniam. 2012. Hunting the chameleon: structural conformations of the intrinsically disordered protein alpha-synuclein. *ChemBioChem* 13(6):761-768.
58. Davidson, W. S., A. Jonas, D. F. Clayton, and J. M. George. 1998. Stabilization of α -synuclein secondary structure upon binding to synthetic membranes. *Journal of Biological Chemistry* 273(16):9443-9449.
59. Bartels, T., J. G. Choi, and D. J. Selkoe. 2011. α -Synuclein occurs physiologically as a helically folded tetramer that resists aggregation. *Nature* 477(7362):107.
60. Luth, E. S., T. Bartels, U. Dettmer, N. C. Kim, and D. J. Selkoe. 2014. Purification of α -synuclein from human brain reveals an instability of endogenous multimers as the protein approaches purity. *Biochemistry* 54(2):279-292.
61. Díaz, N., and D. Suárez. 2007. Molecular dynamics simulations of matrix metalloproteinase 2: role of the structural metal ions. *Biochemistry* 46(31):8943-8952.
62. Banci, L. 2003. Molecular dynamics simulations of metalloproteins. *Current opinion in chemical biology* 7(1):143-149.
63. Wang, Z., H. Sun, C. Shen, X. Hu, J. Gao, D. Li, D. Cao, and T. Hou. 2020. Combined strategies in structure-based virtual screening. *Physical Chemistry Chemical Physics* 22(6):3149-3159.
64. Forli, S., R. Huey, M. E. Pique, M. F. Sanner, D. S. Goodsell, and A. J. Olson. 2016. Computational protein–ligand docking and virtual drug screening with the AutoDock suite. *Nature protocols* 11(5):905-919.
65. Sterling, T., and J. J. Irwin. 2015. ZINC 15–ligand discovery for everyone. *Journal of chemical information and modeling* 55(11):2324-2337.
66. Kamboj, S., C. Harms, L. Kumar, D. Creamer, C. West, J. Klein-Seetharaman, and S. K. Sarkar. 2021. A method of purifying alpha-synuclein in *E. coli* without chromatography. *Heliyon* 7(1):e05874.
67. Zhuang, X., L. E. Bartley, H. P. Babcock, R. Russell, T. Ha, D. Herschlag, and S. Chu. 2000. A single-molecule study of RNA catalysis and folding. *Science* 288(5473):2048-2051.
68. Czerski, J., W. Colomb, F. Cannataro, and S. Sarkar. 2018. Spectroscopic identification of individual fluorophores using photoluminescence excitation spectra. *Journal of microscopy* 270(3):261-271.

69. Colomb, W., J. Czerski, J. Sau, and S. Sarkar. 2017. Estimation of microscope drift using fluorescent nanodiamonds as fiducial markers. *Journal of microscopy* 266(3):298-306.
70. Dittmore, A., J. Silver, S. K. Sarkar, B. Marmer, G. I. Goldberg, and K. C. Neuman. 2016. Internal strain drives spontaneous periodic buckling in collagen and regulates remodeling. *Proceedings of the National Academy of Sciences*:201523228.
71. Sarkar, S. K., B. Marmer, G. Goldberg, and K. C. Neuman. 2012. Single-molecule tracking of collagenase on native type I collagen fibrils reveals degradation mechanism. *Current biology : CB* 22(12):1047-1056.
72. Arnold, B. C. 2014. Pareto distribution. *Wiley StatsRef: Statistics Reference Online*:1-10.

Figures

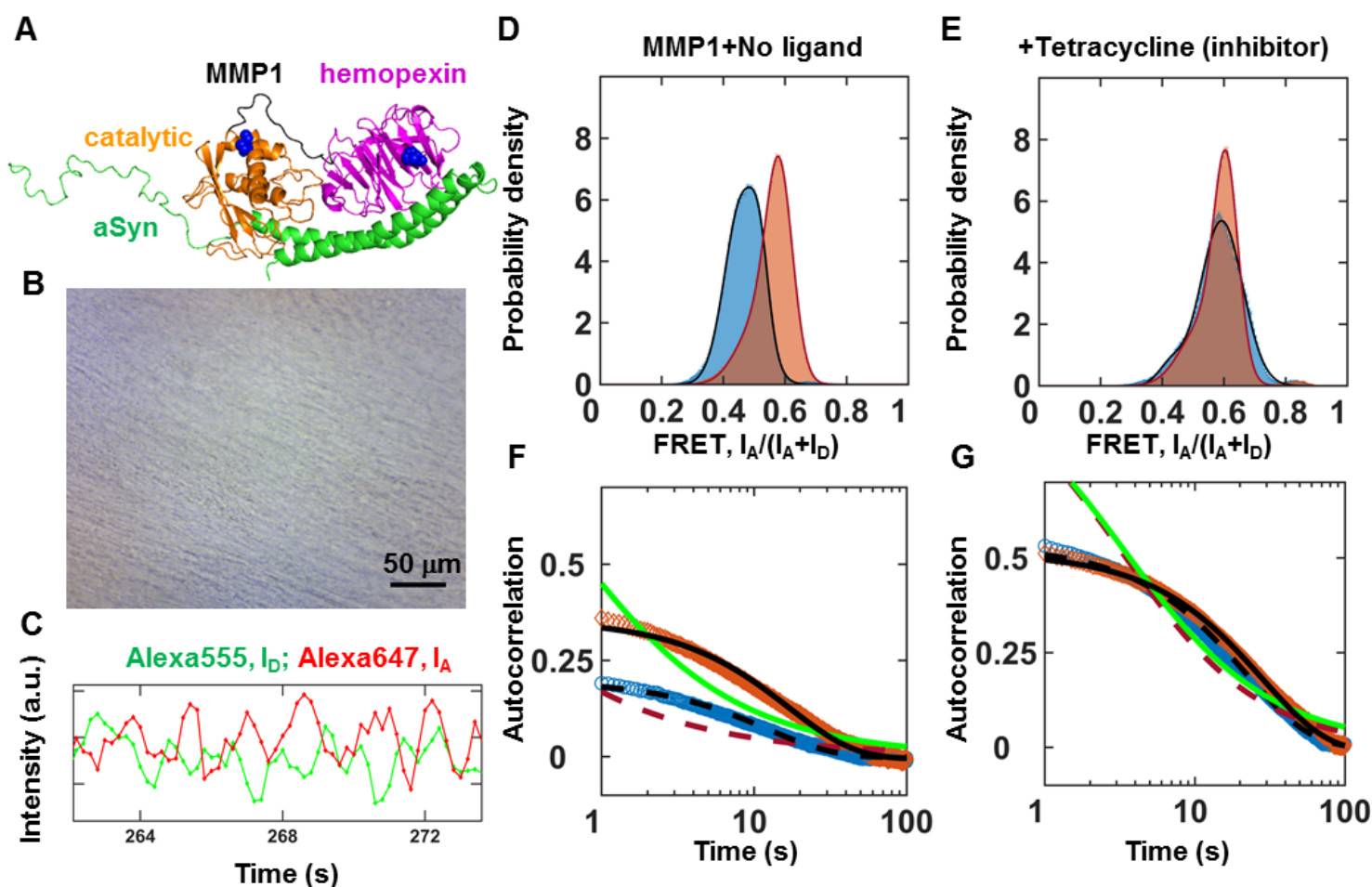


Figure 1

Activity-dependent interdomain dynamics of MMP1 on aSyn-induced aggregates at 22 °C with 100 ms time resolution. (A) One of many predicted binding poses between MMP1 (PDB ID 4AUO; catalytic: orange; linker: black; hemopexin: magenta; S142C and S366C mutations in blue) and aSyn (PDB ID 1XQ8; green). (B) Light microscopy image of aSyn-induced aggregates on a slide. For MMP1-treated

aggregates, see Figure S1. (C) Emission intensities of the two dyes attached to active MMP1. (D) and (E) Area-normalized histograms of MMP1 interdomain distance ($\sim 200,000$ FRET values, bin size=0.005) without ligand and in the presence of tetracycline (an inhibitor), respectively, for active (blue) and inactive (orange) MMP1. All histograms are fitted to a sum of two Gaussians (Equation 1 in methods) (active: solid blue line; inactive: solid red line). (F) and (G) Autocorrelations (Equation 2 in methods) of MMP1 interdomain distance without ligand and in the presence of tetracycline, respectively, for active (blue) and inactive (orange) MMP1. All autocorrelations are fitted to exponentials and power laws (Equation 3 in methods) (exponential fit to active: dashed black line; power law fit to active: dashed red line; exponential fit to inactive: solid black line; power law fit to inactive: solid green line). The error bars in histograms and autocorrelations represent the square roots of the bin counts and the standard errors of the mean (SEM) and are too small to be seen. For best-fit parameters, see Table S1.

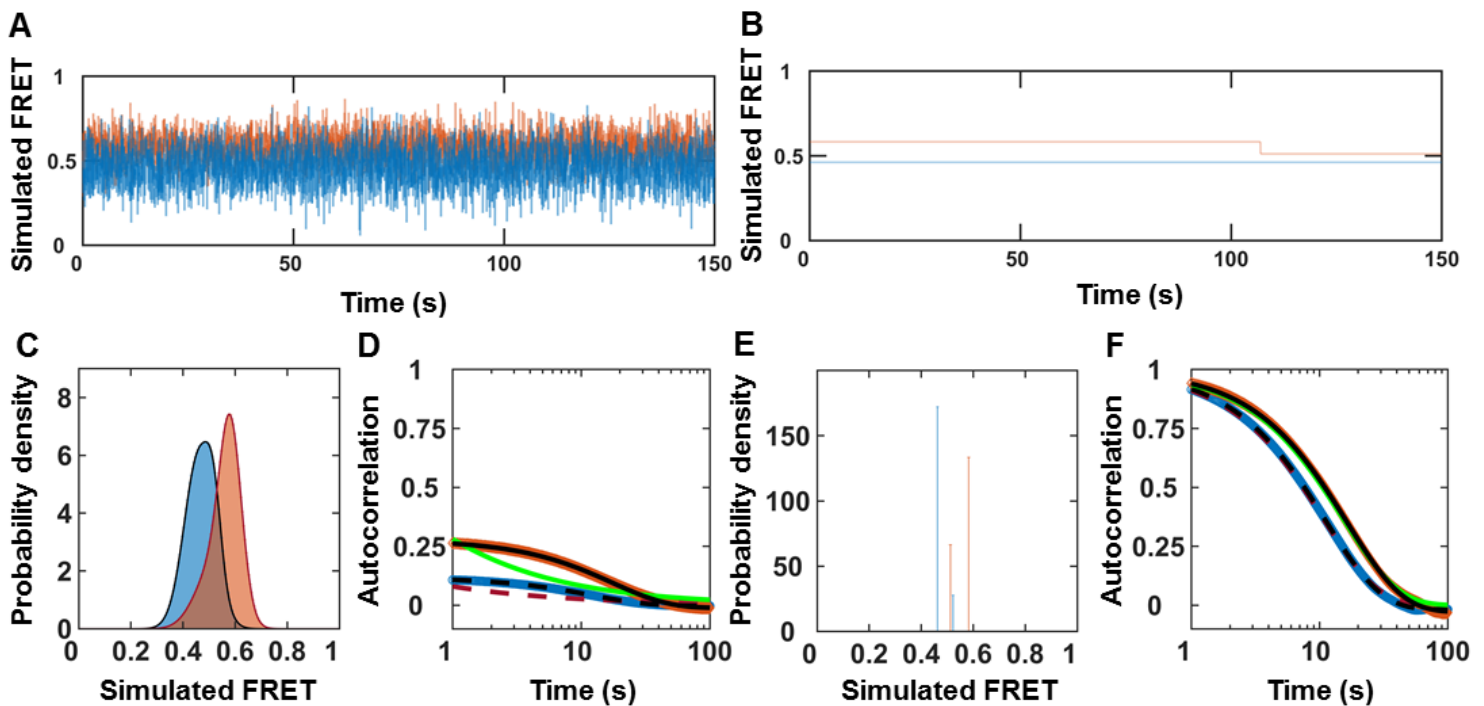


Figure 2

Stochastic simulation of MMP1 interdomain dynamics as a two-state system. (A) and (B) Examples of simulated smFRET trajectories with and without noise, respectively, for active MMP1 (blue) and inactive MMP1 (orange) using experimentally determined parameters for MMP1 without ligands. (C) Area-normalized histograms of simulated smFRET values with noise (active: blue; inactive: orange) with best fits to a sum of two Gaussians (solid line). (D) Autocorrelations of simulated smFRET trajectories with noise (active: blue; inactive: orange) with fits to exponentials (active: dashed black line; inactive: solid black line). Power law does not fit autocorrelations (active: dashed red line; inactive: solid green line). (E) Area-normalized histograms of simulated smFRET values without noise (active: blue; inactive: orange). (F) Autocorrelations of simulated smFRET trajectories without noise (active: blue; inactive: orange) with fits to exponentials (active: dashed black line; inactive: solid black line). Both exponential and power law

fit autocorrelations (active: dashed red line; inactive: solid green line). The error bars are the SEMs for histograms and autocorrelations and are too small to be seen. For best-fit parameters, see Table S2.

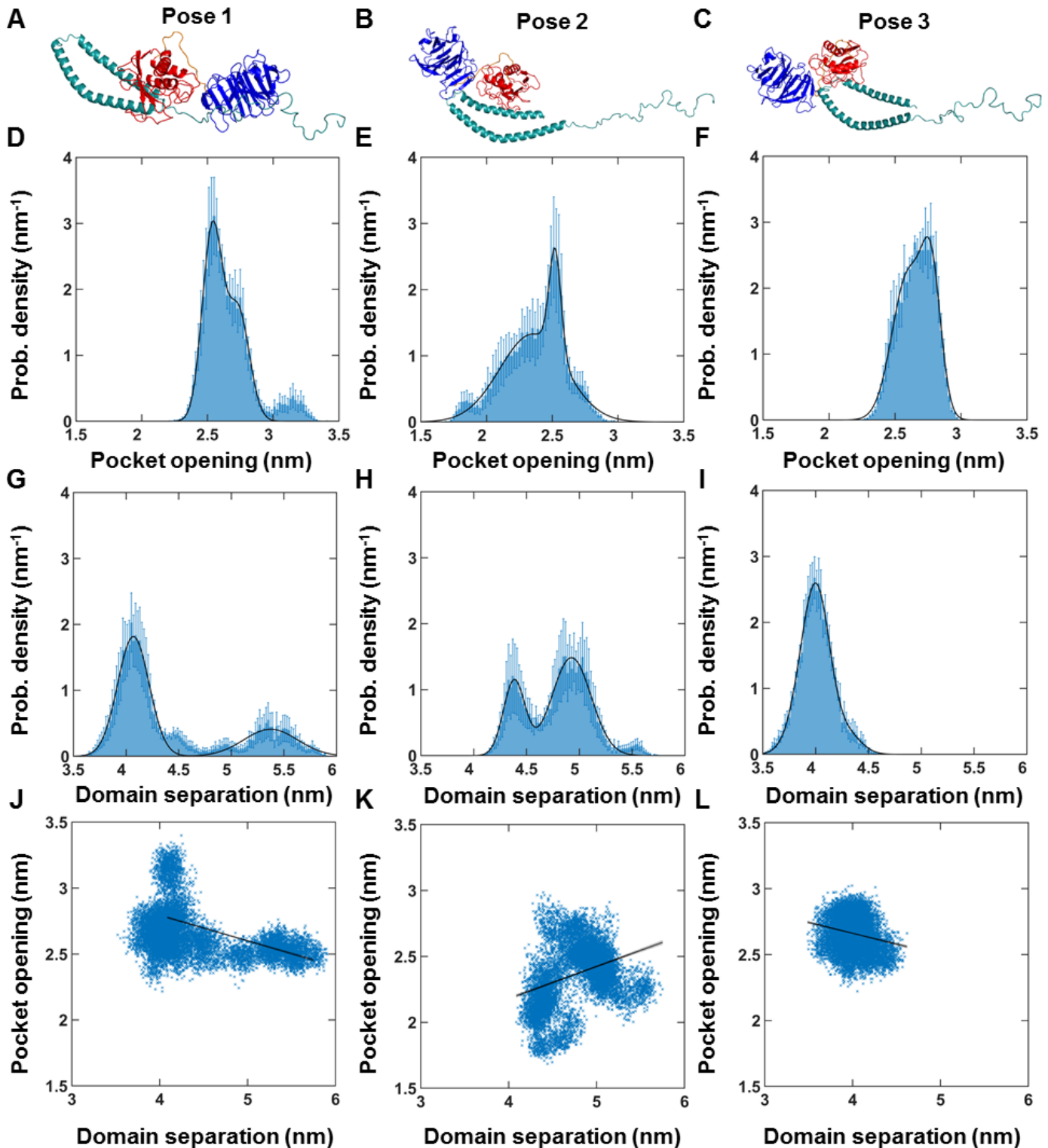


Figure 3

Figure 3. MMP1-aSyn binding pose-dependent dynamics of active MMP1 at 37 °C. (A), (B), and (C) Three binding poses of MMP1 (the catalytic domain in red) at different locations of aSyn. (D), (E), and (F) Area-normalized histograms of the catalytic pocket opening (N171-T230 distance) of MMP1 for poses 1, 2,

and 3, respectively. (G), (H), and (I) Area-normalized histograms of interdomain separation of MMP1 (S142-S366 distance) for poses 1, 2, and 3, respectively. (J), (K), and (L) Linear correlation plots of catalytic pocket opening and interdomain distance for poses 1, 2, and 3, respectively. The data were fitted to (Equation 4 in methods). Note that a larger domain separation corresponds to a lower FRET value. Time resolution=2 fs; Data saved every 5 ps; RMSD stabilization time for MMP1= \sim 5 ns; Total simulation duration=20 ns. For calculations of linear correlations, see methods. For best-fit parameters, see Table S3. The error bars in Figures 3D-I represent the standard deviations of three repeats of simulations for each condition. Figures 3J-L show combined data from the three repeats. We performed two-state simulations with and without noise to study how noise affects the histograms and autocorrelations (Figure 2A-F). Only an exponential fits the autocorrelations with noise (Figure 2D). However, both power law and exponential fit the autocorrelations of simulated smFRET trajectories without noise (Figure 2F). In other words, the presence of noise can convert a power law correlation into an exponential correlation. This effect is similar to converting a Lorentzian line shape into a Gaussian line shape (53). An exponential fit recovers the simulated kinetic rates' underlying sum with and without noise (Table S2).

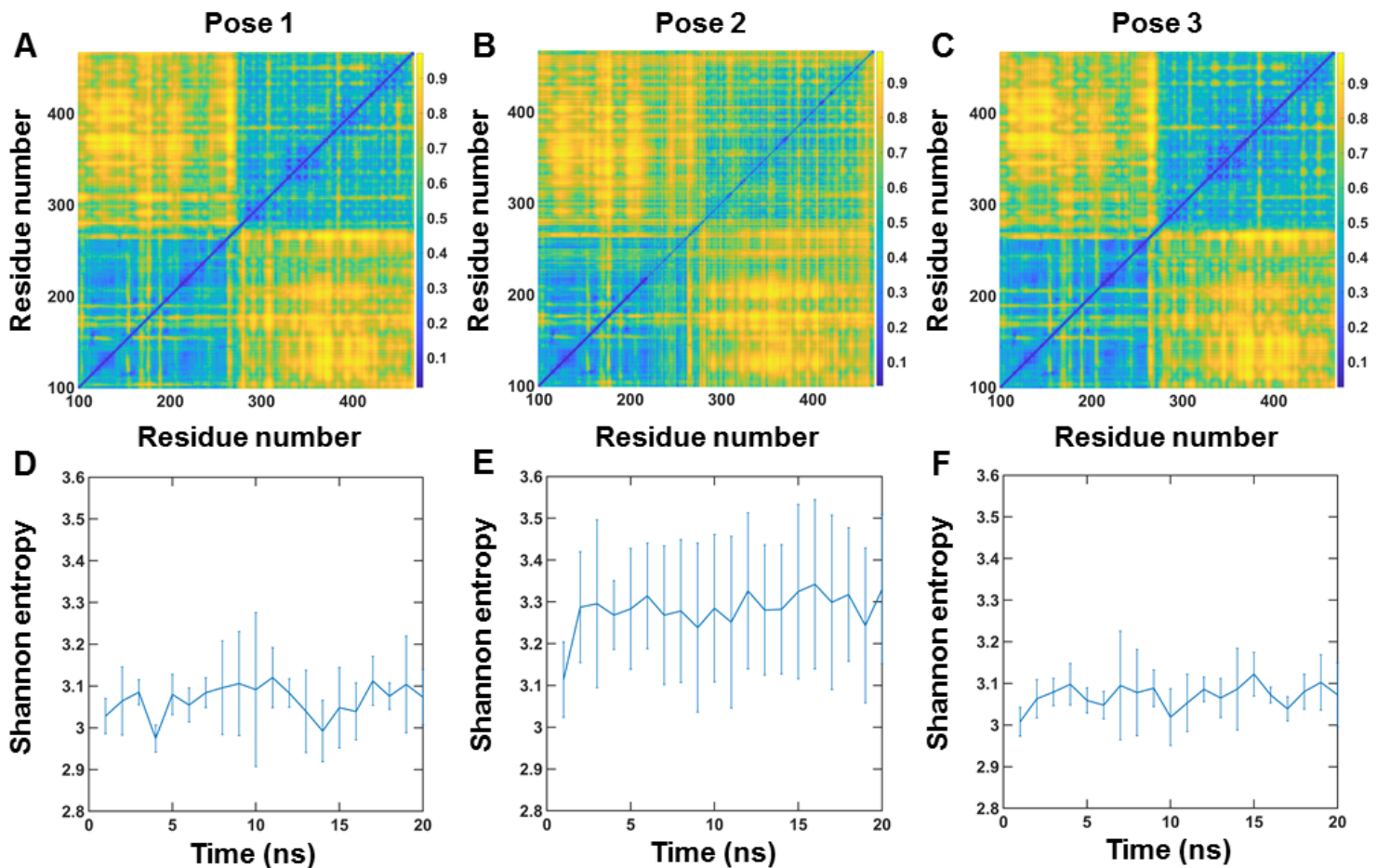


Figure 4

Pose-dependent correlation between residues in active MMP1 and quantification of allostery using Shannon entropy at 37 °C. (A), (B), and (C) Mean correlations between residues in three repeats of simulations for poses 1, 2, and 3, respectively, at 37 °C. Correlations are normalized between 0 (blue) and

1 (yellow). Yellowish colors indicate higher correlations. (D), (E), and (F) Shannon entropy calculated from correlation plots for poses 1 ($S=3.07\pm 0.04$, mean \pm SEM), 2 ($S=3.28\pm 0.05$, mean \pm SEM), and 3 ($S=3.07\pm 0.03$, mean \pm SEM), respectively. For details, see supplementary information and Figure S3. The error bars in Figures 4D-F represent the standard deviations of three repeats of simulations for poses 1, 2, and 3.

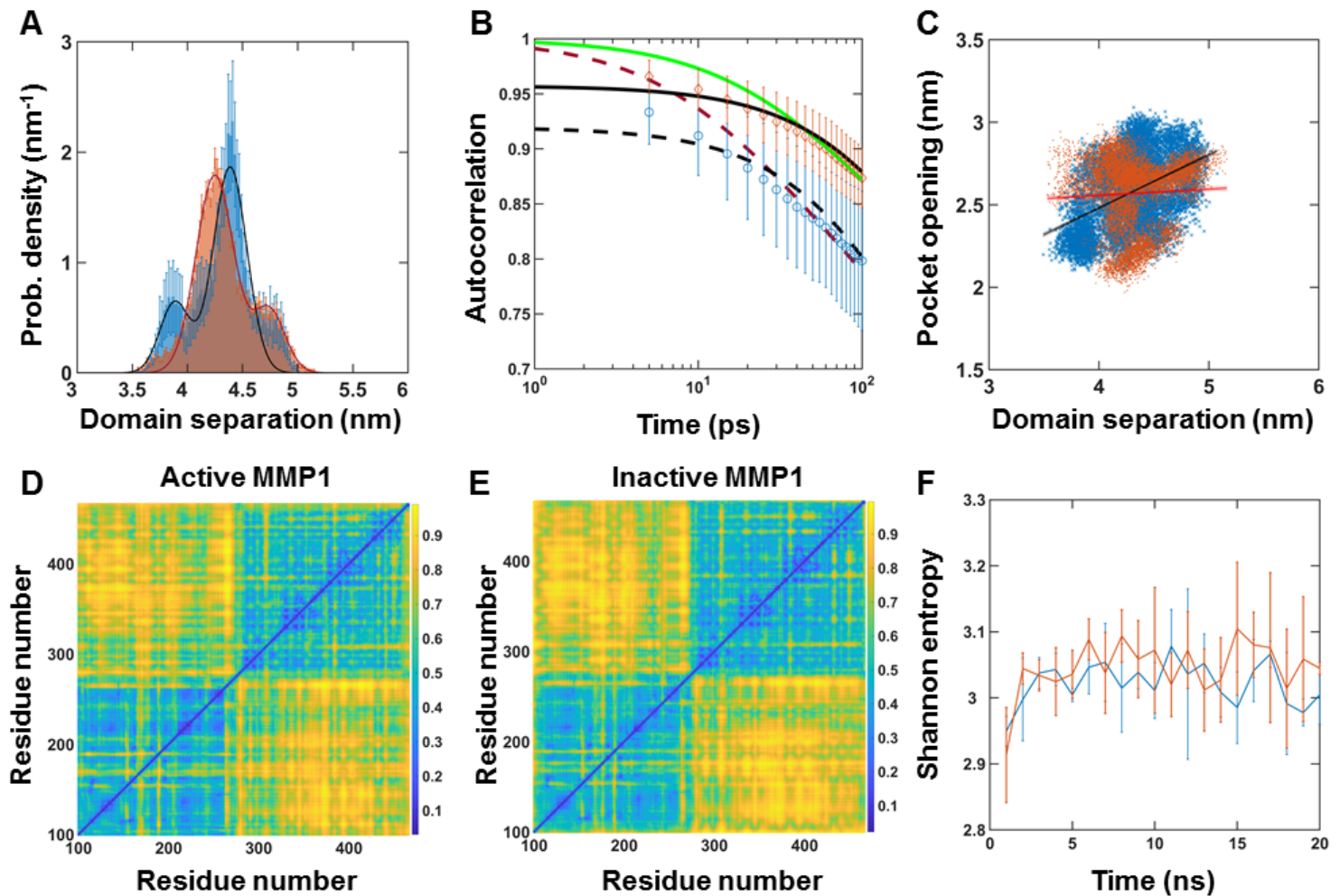


Figure 5

All-atom MD simulation of MMP1 interdomain dynamics of pose 3 at 22 °C. (A) Area-normalized histograms of simulated interdomain distance (active: blue; inactive: orange) with best fits to a sum of two Gaussians (solid line). (B) Autocorrelations of simulated interdomain distance (active: blue; inactive: orange) with fits to exponentials (active: dashed black line; inactive: solid black line). Power law does not fit autocorrelations (active: dashed red line; inactive: solid green line). (C) Linear correlation plots of catalytic pocket opening and interdomain distance. The plot shows combined data from the three repeats of simulations for pose 3. (D) and (E) Mean correlations between residues of three repeats of simulations for pose 3 for active and inactive MMP1, respectively. Correlations are normalized between 0 (blue) and 1 (yellow). Yellowish colors indicate higher correlations. (F) Shannon entropy calculated from correlation plots for active ($S=3.02\pm 0.03$, mean \pm SEM) and inactive ($S=3.04\pm 0.04$, mean \pm SEM). For best-fit

parameters, see Table S4. The error bars in Figures 5A-B and Figure 5F represent the standard deviations of three repeats of simulations for pose 3. Figure 5C shows combined data from the three repeats.

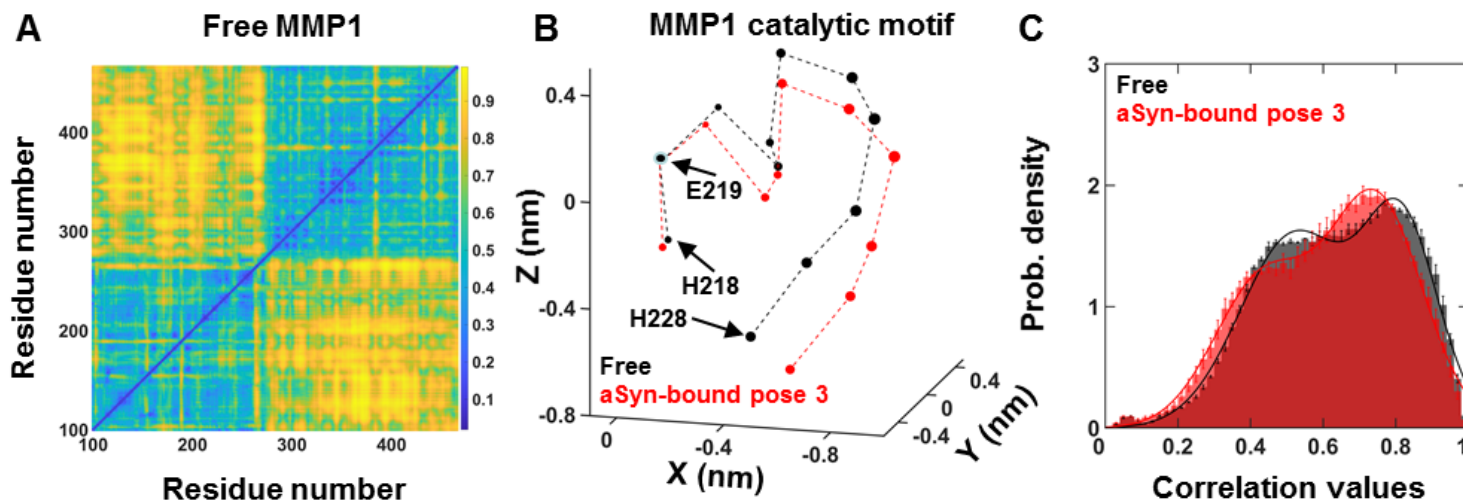


Figure 6

Conformational changes near the catalytic motif and identification of allosteric residues in MMP1 at 37 °C. (A) Normalized correlations between each pair of residue for free active MMP1 at 37 °C. (B) Three-dimensional configurations of the catalytic motif residues for free active MMP1 (black) and aSyn-bound MMP1 (red) at 37 °C. (C) Histograms of correlation values of free MMP1 (black) and aSyn-bound MMP1 (red). For best-fit parameters, see Table S6.

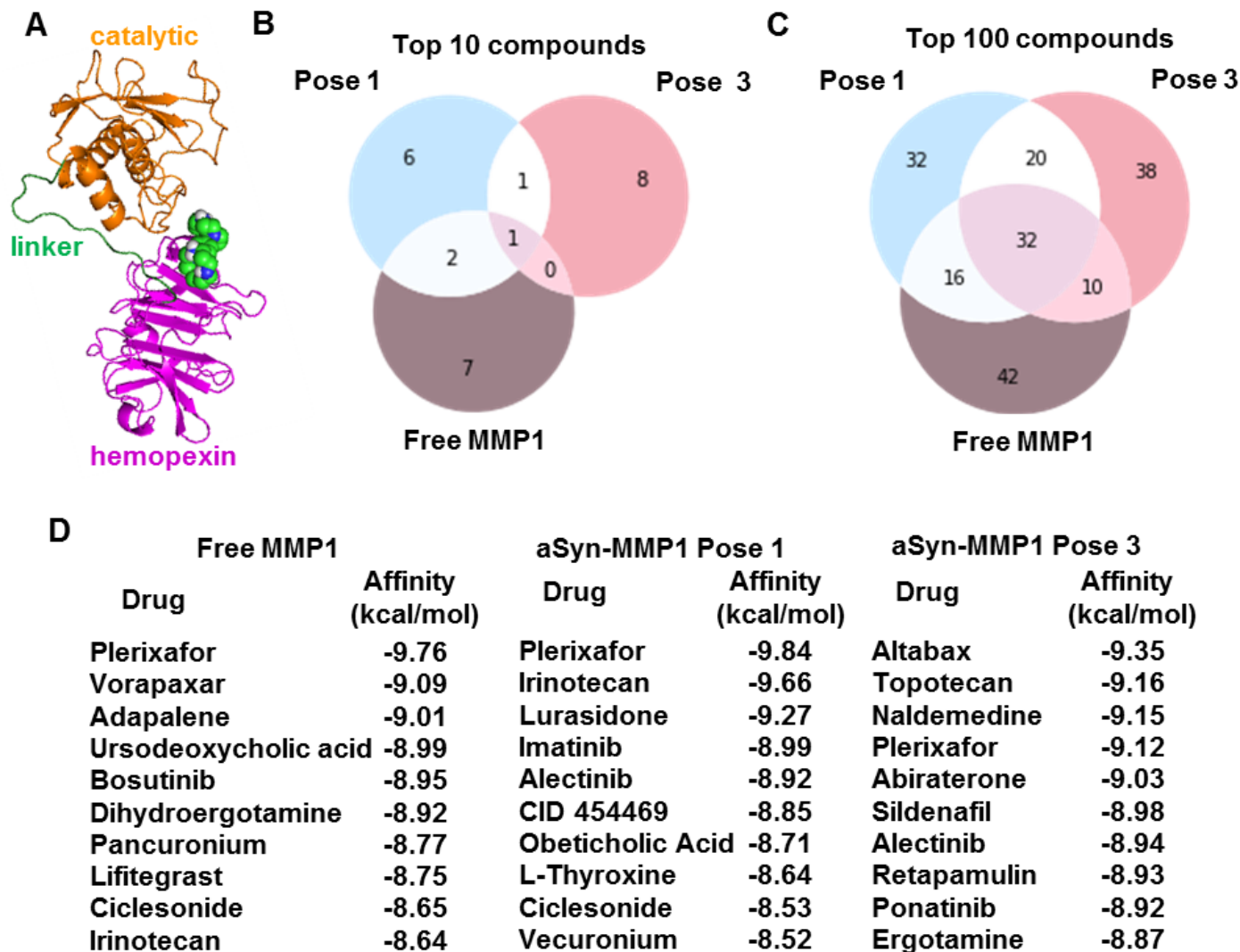


Figure 7

Substrate- and pose-dependent virtual screening against MMP1. (A) MMP1 bound to Plerixafor (green and blue spheres), the top hit against free MMP1. We performed virtual screening against the same site for free MMP1, pose 1, and pose 3. (B) and (C) Venn diagrams of top 10 and 100 molecules show unique and common ligands. (D) Identities and affinities for the top 10 molecules. For docking parameters, see supplementary information.

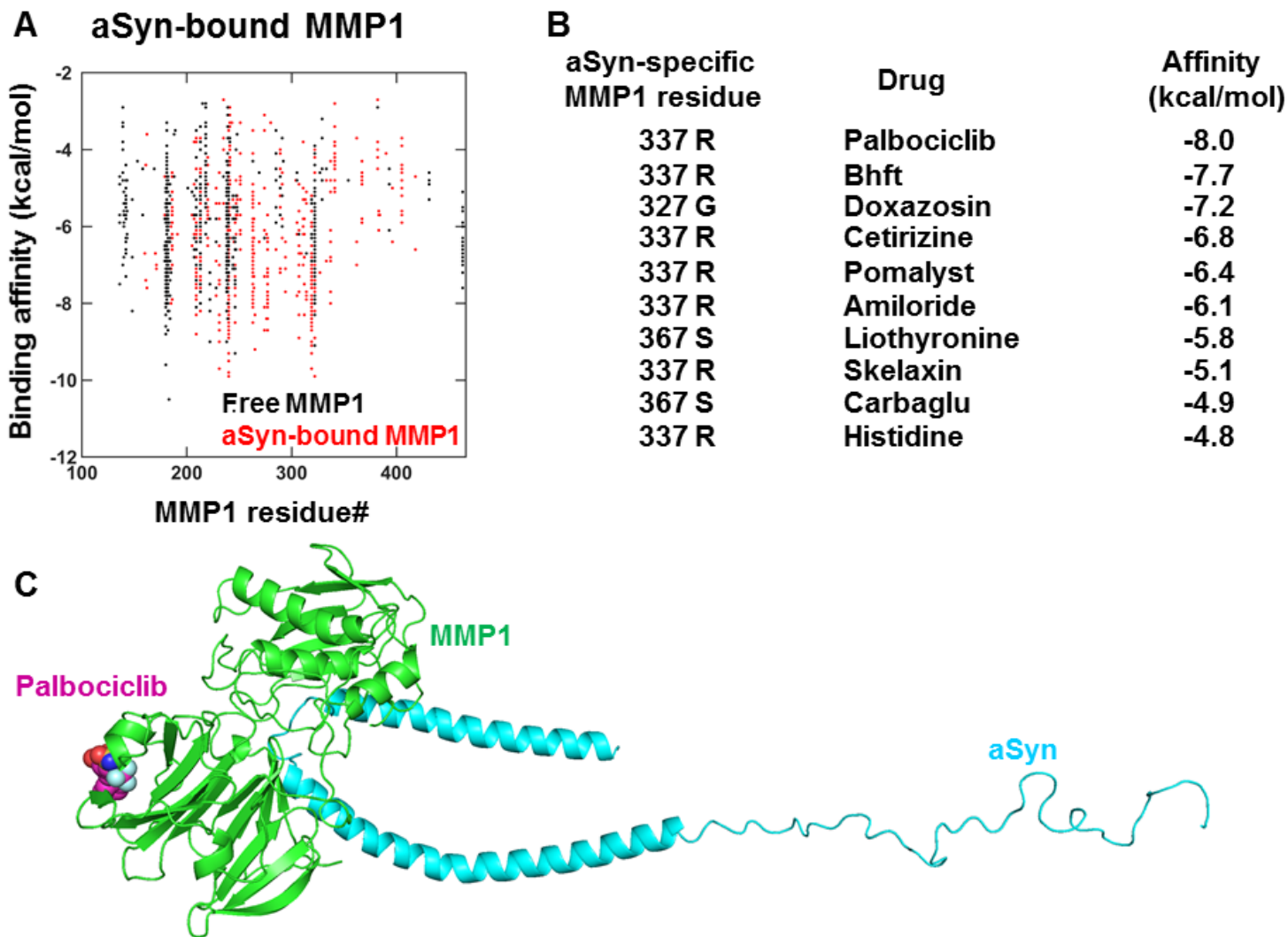


Figure 8

Selection of lead compounds based on substrate-dependent allosteric residues in MMP1. (A) Binding affinities of lead compounds and closest MMP1 residues for aSyn-bound MMP1. (B) Compounds that bind to aSyn-specific allosteric residues in MMP1. (C) Palbociclib bound to aSyn-bound MMP1. Lead molecules depend on whether MMP1 is free or bound to a substrate. Also, not all identified allosteric residues have associated lead molecules. Allosteric residues reduce the number of lead molecules significantly.

Supplementary Files

This is a list of supplementary files associated with this preprint. Click to download.

- [AlphasynucleinMMP1InteractionsSISciRep12032021.pdf](#)